Electrocatalysis Very Important Paper

Deutsche Ausgabe: DOI: 10.1002/ange.201600750
Internationale Ausgabe: DOI: 10.1002/anie.201600750

Pomegranate-Inspired Design of Highly Active and Durable Bifunctional Electrocatalysts for Rechargeable Metal–Air Batteries

*Ge Li⁺, Xiaolei Wang⁺, Jing Fu, Jingde Li, Moon Gyu Park, Yining Zhang, Gregory Lui, and Zhongwei Chen**

Abstract: *Rational design of highly active and durable electrocatalysts for oxygen reactions is critical for rechargeable metal–air batteries. Herein, we report the design and development of composite electrocatalysts based on transition metal oxide nanocrystals embedded in a nitrogen-doped, partially graphitized carbon framework. Benefiting from the unique pomegranate-like architecture, the composite catalysts possess abundant active sites, strong synergetic coupling, enhanced electron transfer, and high efficiencies in the oxygen reduction reaction (ORR) and oxygen evolution reaction (OER). The Co_3O_4-based composite electrocatalyst exhibited a high half-wave potential of 0.842 V for ORR, and a low overpotential of only 450 mV at the current density of 10 mA cm^{-2} for OER. A single-cell zinc–air battery was also fabricated with superior durability, holding great promise in the practical implementation of rechargeable metal–air batteries.*

The fast depletion of fossil fuels and severe deterioration of ecology have stimulated extensive research on the utilization and storage of clean and sustainable energy.[1] Among various energy storage technologies, rechargeable metal–air batteries possess the highest energy density, making them excellent candidates for next generation electrical vehicles (EVs) and hybrid electrical vehicles (HEVs).[2] In metal–air batteries, a metal anode is coupled with an air-breathing cathode that utilizes oxygen from the atmosphere as the reactant for the electrochemical reactions.[3] Discharging and charging processes occur driven by the electrocatalytic oxygen reduction reaction (ORR) and oxygen evolution reduction (OER).[4] The major challenge associated with the commercialization of metal–air batteries resides in the sluggish kinetics of the ORR and OER resulting in large overpotentials.[5] Therefore, developing efficient electrocatalysts with high catalytic activities is of great importance for high performance metal–air batteries.[6]

Precious metal-based catalysts such as platinum (Pt),[7] palladium (Pd),[8] iridium (Ir),[9] and alloys[10] have been intensively studied showing superb catalytic properties and have been widely accepted as the most active electrocatalysts. Unfortunately, the scarcity and electrochemical instability of these catalysts have prevented their widespread use owing to extremely high costs and unsatisfactory durability.[11] Non-precious transition metals (such as Fe, Co, Ni, Mn)[12] and perovskite-based[13] catalysts have been extensively explored.[14] However, they suffer from inefficient catalytic activity owing to self-accumulation and intrinsically poor electrical conductivity. To address these challenges, nanostructured materials with various morphologies (nanoparticles, nanowires, nanosheets, nanotubes) have been designed for effective exposure of catalytic planes and enhanced diffusion of reactive species,[15] while conductive carbon materials (carbon nanotubes (CNTs)[16] and graphene[17]) are often introduced into catalysts to increase the conductivity and structural stability.[18] For example, the Co_3O_4 nanocrystal/reduced graphene oxide bi-functional catalyst exhibits unusual catalytic activity attributed to the synergetic chemical coupling effects.[19] Despite numerous studies, rational design strategy and efficient development of desired high-performance electrocatalysts is yet limited.[20] An efficient electrocatalyst is expected to: i) exhibit high catalytic activity with a large number of active sites for ORR and OER processes; ii) possess sufficient mass transfer pathways for fast electrode kinetics; and iii) be chemically stable with robust material and/or electrode architecture for high durability.[21]

Herein, we demonstrate the development of pomegranate-like electrocatalysts based on transition metal oxide nanocrystals embedded in a nitrogen-doped, partially graphitized carbon framework with excellent catalytic activity for ORR and OER and outstanding durability. Nitrogen-doping has been reported to remarkably accelerate the OER process by participating in the electrocatalytic reaction.[22] To demonstrate the design concept, cobalt oxide (Co_3O_4) was chosen as a model material owing to its abundance and theoretically high electrocatalytic activity.[23] As illustrated in Scheme 1, the Co_3O_4 nanocrystals embedded nitrogen-doped, partially graphitized carbon framework (Co_3O_4/NPGC) with unique pomegranate-like composite architecture provides several major advantages: i) low dimension of highly active Co_3O_4 nanocrystals seeds possess active sites for electrochemical reactions; ii) the pomegranate-like structure efficiently prevents the metal oxide from self-accumulation and provide the mass transfer pathways, which further maintains the catalytic activity; iii) graphitized carbon shell and framework is not only highly conductive, which significantly increases electrical conductivity (Supporting Information, Figure S1), but also

---

[*] Dr. G. Li,[+] Dr. X. Wang,[+] J. Fu, Dr. J. Li, M. G. Park, Dr. Y. Zhang, G. Lui, Prof. Z. Chen
Department of Chemical Engineering
Waterloo Institute for Nanotechnology
Waterloo Institute for Sustainable Energy
University of Waterloo
200 University Avenue West, Waterloo, Ontario, N2L 3G1 (Canada)
E-mail: zhwchen@uwaterloo.ca

[+] These authors contributed equally to this work.

Supporting information and the ORCID identification number(s) for the author(s) of this article can be found under: http://dx.doi.org/10.1002/anie.201600750.

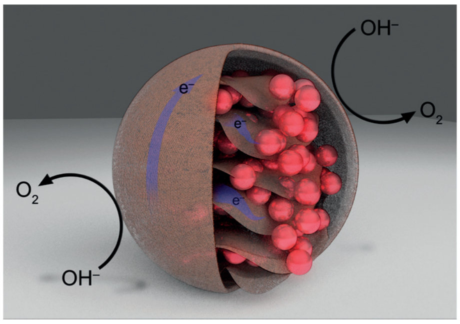

Scheme 1. Illustration of the bifunctional electrocatalyst of Co_3O_4 nanocrystals embedded in a nitrogen-doped partially graphitized carbon framework with unique pomegranate-like composite architecture.

chemically stable and highly robust, which enhances the durability of the catalyst.

The morphology of the Co_3O_4/NPGC was characterized by scanning electron microscopy (SEM). Figure 1 A shows a representative SEM image of as-synthesized nanocomposites that possess spherical morphology with smooth surface and uniform size. High-magnification SEM images (Figure 1 B) clearly displays the spheres with an average diameter of around 300 nm. The structure of the Co_3O_4/NPGC nanocomposites was revealed by transmission electron microscopy (TEM). Figure 1 C shows a representative TEM image of the nanocomposites where three spheres can be observed. A pomegranate-like composite architecture was found with clusters of seeds encapsulated within the carbon framework. High-resolution TEM (HRTEM) images revealed that the carbon framework is highly graphitized owing to the presence of cobalt. The graphitization occurs not only on the surface (Figure 1 D), but also within the whole composite spheres (Figure 1 E), forming highly conductive carbon networks. It is worth mentioning that the carbon framework is still porous, which provides sufficient pathways to facilitate mass transfer. The encapsulated seeds, with an average size of ≈10 nm, were highly crystalline and could be indexed to cubic Co_3O_4 where the (220) plane is exposed (Figure 1 F and G).[24] These nanocrystals have intimate contact with the highly conductive graphitized carbon framework, which significantly improves the conductivity of the composite electrochemical catalyst. The pomegranate-like structure was further revealed by high-angle annular dark field (HAADF) scanning TEM (STEM) image (Figure 1 H), where the nanocrystals seeds were assembled and encapsulated within the carbon framework. The corresponding energy-dispersive X-ray spectroscopy (EDS) mapping (Figure 1 I) confirmed the presence of elements Co, O, C, and N. The homogeneous dispersion of C and N indicated the successful N-doping, while the uniformly distribution of Co and O confirmed the formation of cobalt oxides.

Nitrogen adsorption/desorption analysis was used to examine the pore structure of the Co_3O_4/NPGC. As shown in Figure 2 A, a type-IV isotherm is obtained, suggesting the coexistence of mircropores and mesopores.[25] The pore size distribution (Figure 2 A, inset) confirms the hierarchically

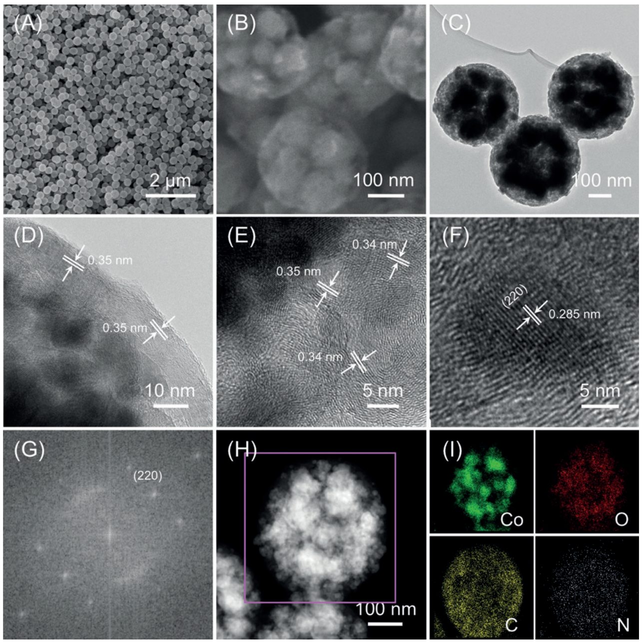

Figure 1. A) Low- and B) High-magnification SEM images of as-synthesized Co_3O_4/NPGC. C) TEM image of three Co_3O_4/NPGC composite spheres. D) HRTEM image of partially graphitized carbon on the edge of a composite sphere. E) HRTEM image of partially graphitized carbon within a composite sphere. F) HRTEM image of a single Co_3O_4 nanocrystal embedded within Co_3O_4/NPGC. G) The corresponding FFT diffraction pattern of the single Co_3O_4 nanocrystal. H) HAADF-STEM image of the Co_3O_4/NPGC, and I) the corresponding element mapping spectra on Co, O, C, and N.

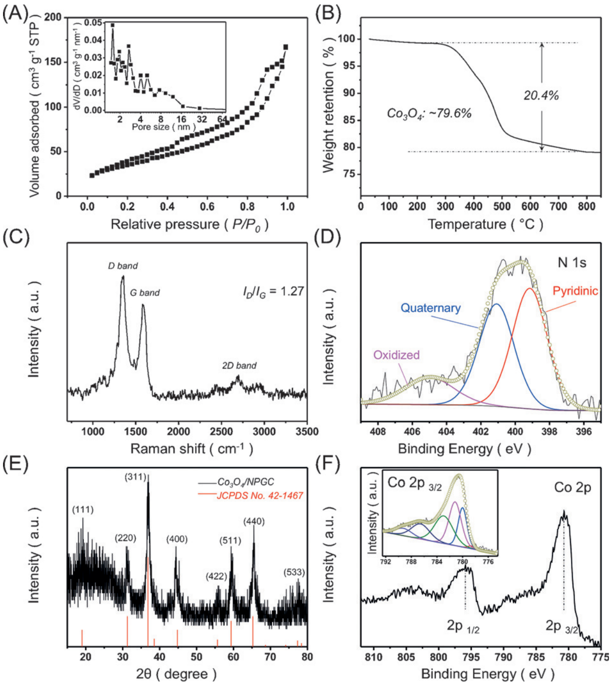

Figure 2. A) N_2 adsorption/desorption isotherms and pore size distribution, B) TGA profile, and C) Raman spectrum of the Co_3O_4/NPGC. D) Core-level scan XPS spectrum of element N in the nanocomposites. E) XRD pattern of the Co_3O_4/NPGC. F) Core-level scan XPS spectrum of element Co in the nanocomposites.

porous structure that is mainly originated from the assembly of Co_3O_4 nanocrystals. The nanocomposites possess a high Brunauer–Emmett–Teller (BET) surface area of 145 $m^2 g^{-1}$ which provides high density of active sites for redox reactions, and a Barrett–Joyner–Halenda (BJH) pore volume of 0.24 $cm^3 g^{-1}$ which favors the mass transfer. According to the thermogravimetric analysis (Figure 2B), the Co_3O_4 content in Co_3O_4/NPGC was calculated to be 79.6%, while the carbon content was 20.4%. The carbon framework was clearly highly graphitized (Figure 2C), with an I_D/I_G ratio of 1.27. To further determine the chemical composition of the nanocomposites, X-ray photoelectron spectroscopy (XPS) analysis was performed (Figure S2). The presence of the element N indicated the successful incorporation of N into the graphitic matrix with a N-doping content of 2.94%. Figure 2D shows the core-level scan spectrum of N 1s that can be interpreted into three characteristic peaks located at 398.88, 400.81, and 404.69 eV, corresponding to three main nitrogen species (pyridinic, quaternary, and nitrogen oxides)[26] with the content of 46.18, 39.31, and 14.51%, respectively. Note that both pyridinic and quaternary N-dopants possess the electron-accepting ability which creates net positive charges on adjacent carbon atoms to facilitate oxygen adsorption for ORR with low overpotential.[27] The X-ray diffraction pattern of the nanocomposites (Figure 2E) further confirmed the formation of cubic Co_3O_4 (JCPDS No. 42-1467).[28] The crystal domain size was estimated to be 9.68 nm using Sherrer's equation, which is consistent with the HRTEM observations. Figure 2F depicts the core-level scan spectrum of Co 2p, which exhibits a doublet at 795.87 and 780.75 eV, confirming the presence of Co with mixed valence. The Co $2p_{3/2}$ spectrum (Figure 2F, inset) can be deconvoluted into several peaks, of which the peaks with binding energies of 781.21 and 779.99 eV can be attributed to nitrogen- and oxygen-coordinated Co, respectively, implying the formation of Co–N and Co–O structures that exhibit considerable catalytic activity.[29]

The Co_3O_4/NPGC nanocomposites possess unique pomegranate-like architecture for improved catalytic performance. The electrocatalytic activity of the Co_3O_4/NPGC for ORR was first investigated by linear sweep voltammetry (LSV) in O_2-saturated 0.1M KOH electrolyte using a three-electrode system. Commercial Co_3O_4 nanoparticles, with an average size of 50 nm, and the nanocomposite without N-doping (Co_3O_4/PGC) were also measured for comparison. The polarization curves of different catalysts at a scan rate of 10 $mV s^{-1}$ and a rotation speed of 1600 rpm are shown in Figure 3A. The Co_3O_4/PGC showed an onset potential of 0.93 V (vs. reversible hydrogen electrode, RHE) and diffusion-limited current density of -4.45 $mA cm^{-2}$, which is similar to the commercial Co_3O_4 nanoparticles (0.93 V vs. RHE and -4.55 $mA cm^{-2}$). By comparison, the Co_3O_4/NPGC exhibited a pronounced improvement in ORR activity, with its more positive onset potential of 0.97 V and significantly larger diffusion-limited current density of -5.84 $mA cm^{-2}$. Additionally, the more positive half-wave potential of Co_3O_4/NPGC ($E_{1/2} = 0.842$ V) compared with that of the commercial Co_3O_4 nanoparticles (0.68 V) and the Co_3O_4/PGC (0.69 V) suggests a synergistic ORR activity of Co_3O_4 and N-doped GC in the nanocomposite. Note that quaternary N can induce non-uniform electron density distribution on adjacent carbon atoms and facilitate O_2 adsorption and dissociation, thus functioning as the efficient active site of ORR. To further investigate the ORR kinetics of the Co_3O_4/NPGC electrocatalyst, polarization curves were obtained at various rotation speeds ranging from 400 to 2500 rpm. As shown in Figure 3B, the Co_3O_4/NPGC exhibited a well-defined platform of diffusion-limited currents at all rotational speeds. More importantly, the near parallelism of the fitted lines suggests first-order reaction kinetics toward the concentration of dissolved oxygen. Based on the Koutecky–Levich (K-L) equation where the corresponding K-L curves were plotted by the inverse current density (J^{-1}) versus the inverse of the square root of the rotation speed ($\omega^{1/2}$) at various electrode potentials (-0.45, -0.50, -0.55, and -0.60 V vs. SCE; Figure 3C), the number of electrons (n) transferred during ORR is estimated to be ≈ 4.0. The linearity of the K-L plot and the n value indicate fast kinetics with a predominant four-electron reduction reaction mechanism throughout the entire potential range inspected. As mentioned above, the graphitization occurs not only on the surface, but also within the whole nanocomposites during synthesis, which leads to a highly conductive carbon framework contributing the fast ORR process.

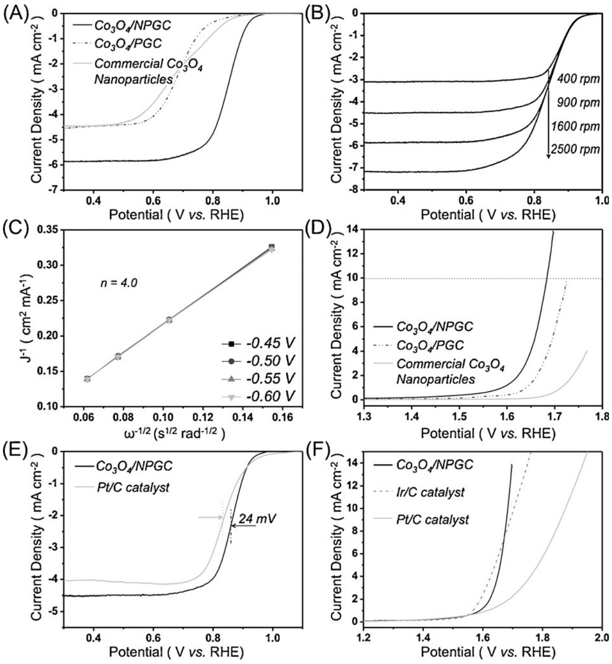

Figure 3. A) Comparison of ORR polarization curves of Co_3O_4/NPGC, Co_3O_4/PGC, and commercial Co_3O_4 nanoparticles electrocatalysts. B) ORR polarization curves of Co_3O_4/PGC at different rotating speeds (400 to 2500 rpm). C) K-L plot of Co_3O_4/NPGC. D) Comparison of OER polarization curves of Co_3O_4/NPGC, Co_3O_4/PGC, and commercial Co_3O_4 nanoparticles electrocatalysts. Comparison of E) ORR polarization curves of Co_3O_4/NPGC and Pt/C catalysts at 900 rpm, and F) OER polarization curves of Co_3O_4/NPGC, Ir/C, and Pt/C catalysts.

To assess the bifunctionality of the Co_3O_4/NPGC nanocomposites catalyst, the catalytic activity for OER was also investigated. Figure 3D compares the LSV behavior of as-prepared Co_3O_4/NPGC, Co_3O_4/PGC, and commercial Co_3O_4

nanoparticles catalysts in the voltage range from 0 to 0.8 V (vs. RHE) at a scan rate of 10 mV s^{-1} and a rotation speed of 900 rpm in N_2-saturated 0.1 M KOH. As expected, the Co_3O_4/NPGC showed the lowest overpotential of only 450 mV at the current density of 10 mA cm^{-2}, compared to the overpotentials of Co_3O_4/PGC (495 mV) and commercial Co_3O_4 (> 600 mV). We believed that with the help of nitrogen doping, more Co_3O_4 active sites could be exposed and participate in the reaction. The synergistic combination of Co_3O_4 NCs and nitrogen-doped partially graphitized carbon can significantly improve the catalytic activity of this material. The ORR and OER activities of these three materials are summarized in Table S1.

Remarkably, Co_3O_4/NPGC shows outstanding catalytic performance even compared to those precious metal catalysts. As shown in Figure 3E, Co_3O_4/NPGC exhibits a 24 mV higher half-wave potential than the Pt/C catalyst, which is considered as the best electrocatalyst for ORR at a rotation speed of 900 rpm. For the OER process, although Ir/C, one of the best OER electrocatalysts, possesses a slightly more negative onset potential, the Co_3O_4/NPGC exhibits a steeper polarization curve, indicating that the unique pomegranate-like architecture along with the synergistic coupling significantly improves the reaction kinetics.

To better understand this extraordinary catalytic property, we correlated the performance with the architecture of the nanocomposites where the (220) or (110) planes of Co_3O_4 nanocrystals were preferably exposed (Figure S3) by calculating the free energies based on density functional theory (Figure S4). Figure 4 compares how the free energy changes at the (110) (Figure 4A) and (111) (Figure 4B) planes of cubic Co_3O_4 nanocrystals in each step during the OER process at zero electrode potential ($\Phi = 0$ V vs. RHE) and reversible potential for each intermediate reaction. At the equilibrium potential (U = 1.23 V), on Co_3O_4 (110) surface, OH* and O* formation is energetically downhill (exothermic), whereas all of the other steps are uphill (endothermic). On the Co_3O_4 (111) surface, OH* and O_2 formation is energetically downhill, whereas all of the other steps are uphill at $U = 1.23$ V. By applying an overpotential $U > 1.23$ V, all of the free energy steps of OER intermediates become relatively more negative at potentials 2.37 and 3.60 V (vs. RHE) for (110) and (111) planes, respectively. Significantly lower overpotentials are obtained from the Co_3O_4 (110) surface compared to the Co_3O_4 (111) surface, clearly indicating that Co_3O_4 (110) has superior OER activity.

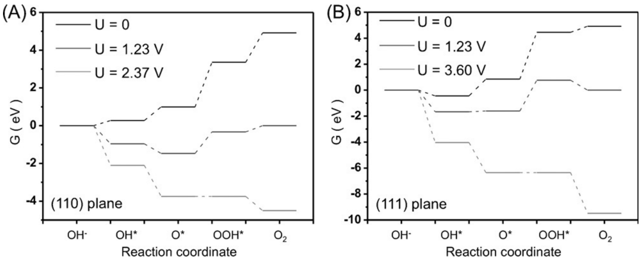

Figure 4. Standard free energy diagrams for OER obtained at zero potential ($U = 0$), equilibrium potential for OER ($U = 1.23$ V), and at the potential for which all steps proceed downward at pH 14 and $T = 298$ K.

To explore the feasibility of the pomegranate-structured electrocatalyst for future practical applications, a single-cell practical zinc–air battery was assembled using the Co_3O_4/NPGC nanocomposites as the active air electrode material and oxygen in atmospheric air as the main source of fuel (Figure 5A). Figure 5B shows the galvanodynamic behaviors of the Co_3O_4/NPGC nanocomposite electrocatalyst during battery charge and discharge processes. The zinc–air battery using Co_3O_4/NPGC composite electrocatalyst exhibited comparable discharge performance to Pt/C catalyst at relatively lower current densities, and significantly outperformed the zinc–air battery using Pt/C catalyst at relatively higher current densities, which is consistent with the performance comparison in half-cells (Figure S5). The excellent single-cell zinc–air battery performance clearly shows its cost competitiveness over precious-metal-based commercial catalysts. Moreover, compared to the durability of commercial Ir/C (Figure 5C) and Pt/C (Figure 5D), the Co_3O_4/NPGC electrocatalyst exhibits significantly improved durability (Figure 5E) with virtually no voltage fading for both the discharge and charge process even more than 80 h of continuous operation. Interestingly, the discharge overpotential is progressively

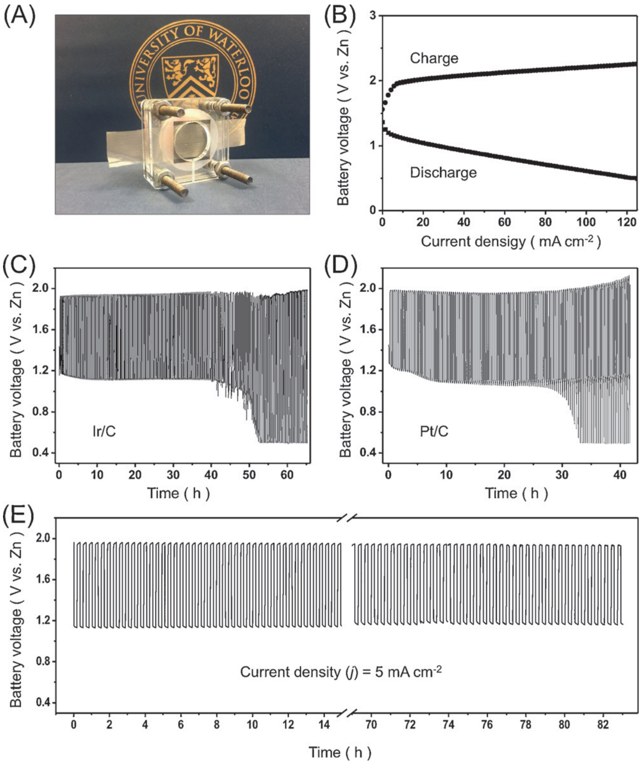

Figure 5. A) Configuration of the single-cell zinc–air battery. B) Galvanodynamic charge–discharge profile of the rechargeable zinc–air battery with Co_3O_4/NPGC nanocomposites electrocatalyst. Galvanostatic charge–discharge cycling performance of rechargeable zinc–air batteries with C) commercial Ir/C, D) commercial Pt/C, and E) Co_3O_4/NPGC nanocomposites electrocatalysts, respectively.

improved as the cycling proceeds, which may be attributed to the unique composite architecture where the catalyst is gradually activated. In contrast, both the state-of-the-art Ir/C and Pt/C catalysts provide inferior cycle stability with operation time of less than 45 h (Figure 5C) and 30 h (Figure 5D), respectively, resulting in a significant discharge and charge performance losses. The superior performance of the Co_3O_4/NPGC electrocatalyst is mainly attributed to the unique composite architecture. On the one hand, the partially graphitized carbon frame not only is robust enough for repeated cycling, but also provides sufficient protection for highly active Co_3O_4 nanocrystals. On the other hand, the N dopants coupling with Co_3O_4 nanocrystals efficiently enhance the integrity of the composite spheres, enabling a long cycling stability.

In summary, a pomegranate-like electrocatalyst has been successfully designed and characterized based on transition metal oxide nanocrystals embedded in a nitrogen-doped, partially graphitized carbon framework. The electrocatalysts using Co_3O_4 nanocrystals exhibit excellent catalytic activity for ORR and OER, and outstanding durability owing to the unique pomegranate composite architecture, where low-dimension nanocrystal seeds possess highly active sites for electrochemical reactions, and the graphitized carbon shell and framework significantly increases the electrical conductivity and structural stability. Moreover, the pomegranate-like structure efficiently prevents the metal oxide from self-accumulation and provides the mass transfer pathways, which further maintains the catalytic activity. The excellent single-cell zinc–air battery performance is achieved with superior durability, holding great promise in the practical implementation of rechargeable metal–air batteries.

Acknowledgements

This work was financially supported by the Natural Sciences and Engineering Research Council of Canada (NSERC), the University of Waterloo, and the Waterloo Institute for Nanotechnology. The authors would like to acknowledge the Canadian Center for Electron Microscopy (CCEM) at McMaster University for TEM and HAADF-STEM support, and the Shared Hierarchical Academic Research Computing Network and Compute/Calcul Canada for the access to the facilities.

Keywords: bifunctional catalyst · Co_3O_4 nanocrystals · DFT calculations · metal–air battery · pomegranate-like architecture

How to cite: *Angew. Chem. Int. Ed.* **2016**, *55*, 4977–4982
Angew. Chem. **2016**, *128*, 5061–5066

---

[1] a) Y. Liang, Y. Li, H. Wang, H. Dai, *J. Am. Chem. Soc.* **2013**, *135*, 2013–2036; b) M. S. Whittingham, *MRS Bull.* **2008**, *33*, 411–419; c) M. Armand, J. M. Tarascon, *Nature* **2008**, *451*, 652–657.

[2] a) P. G. Bruce, S. A. Freunberger, L. J. Hardwick, J.-M. Tarascon, *Nat. Mater.* **2012**, *11*, 19–29; b) Q. Huang, W. Cai, H. Yang, J. Liu, J. Cai, R. Xiong, X. Yu, R. Js, A. P. Shapiro, R. L. Hart, C. Wei, *ECS Trans.* **2009**, *16*, 35–45; c) F. Cheng, J. Chen, *Chem. Soc. Rev.* **2012**, *41*, 2172–2192.

[3] a) M. D. Radin, D. J. Siegel, *Energy Environ. Sci.* **2013**, *6*, 2370–2379; b) G. Girishkumar, B. McCloskey, A. C. Luntz, S. Swanson, W. Wilcke, *J. Phys. Chem. Lett.* **2010**, *1*, 2193–2203.

[4] J.-S. Lee, S. Tai Kim, R. Cao, N.-S. Choi, M. Liu, K. T. Lee, J. Cho, *Adv. Energy Mater.* **2011**, *1*, 34–50.

[5] a) F. Cheng, J. Liang, Z. Tao, J. Chen, *Adv. Mater.* **2011**, *23*, 1695–1715; b) M. G. Walter, E. L. Warren, J. R. McKone, S. W. Boettcher, Q. Mi, E. A. Santori, N. S. Lewis, *Chem. Rev.* **2010**, *110*, 6446–6473; c) D. Higgins, P. Zamani, A. Yu, Z. Chen, *Energy Environ. Sci.* **2016**, *9*, 357–390.

[6] B. Y. Xia, Y. Yan, N. Li, H. B. Wu, X. W. Lou, X. Wang, *Nat. Energy* **2016**, *1*, 15006.

[7] a) Y.-C. Lu, Z. Xu, H. A. Gasteiger, S. Chen, K. Hamad-Schifferli, Y. Shao-Horn, *J. Am. Chem. Soc.* **2010**, *132*, 12170–12171; b) T. Yu, D. Y. Kim, H. Zhang, Y. Xia, *Angew. Chem. Int. Ed.* **2011**, *50*, 2773–2777; *Angew. Chem.* **2011**, *123*, 2825–2829.

[8] a) C. W. Xu, H. Wang, P. K. Shen, S. P. Jiang, *Adv. Mater.* **2007**, *19*, 4256–4259; b) M.-H. Shao, K. Sasaki, R. R. Adzic, *J. Am. Chem. Soc.* **2006**, *128*, 3526–3527.

[9] Y. Lee, J. Suntivich, K. J. May, E. E. Perry, Y. Shao-Horn, *J. Phys. Chem. Lett.* **2012**, *3*, 399–404.

[10] a) B. Lim, M. Jiang, P. H. C. Camargo, E. C. Cho, J. Tao, X. Lu, Y. Zhu, Y. Xia, *Science* **2009**, *324*, 1302–1305; b) Z. Peng, H. Yang, *J. Am. Chem. Soc.* **2009**, *131*, 7542–7543.

[11] a) Y. Shao, G. Yin, Y. Gao, *J. Power Sources* **2007**, *171*, 558–566; b) R. Bashyam, P. Zelenay, *Nature* **2006**, *443*, 63–66; c) Y. Gorlin, T. F. Jaramillo, *J. Am. Chem. Soc.* **2010**, *132*, 13612–13614.

[12] a) M. Gong, Y. Li, H. Wang, Y. Liang, J. Z. Wu, J. Zhou, J. Wang, T. Regier, F. Wei, H. Dai, *J. Am. Chem. Soc.* **2013**, *135*, 8452–8455; b) G. Wu, K. L. More, C. M. Johnston, P. Zelenay, *Science* **2011**, *332*, 443–447; c) J. Xu, P. Gao, T. S. Zhao, *Energy Environ. Sci.* **2012**, *5*, 5333–5339; d) H. Tüysüz, Y. Hwang, S. Khan, A. Asiri, P. Yang, *Nano Res.* **2013**, *6*, 47–54; e) M. Augustin, O. Yezerska, J. Derendorf, M. Knipper, D. Fenske, T. Plaggenborg, J. Parisi, *ECS Trans.* **2013**, *45*, 1–10.

[13] a) W. G. Hardin, D. A. Slanac, X. Wang, S. Dai, K. P. Johnston, K. J. Stevenson, *J. Phys. Chem. Lett.* **2013**, *4*, 1254–1259; b) J.-I. Jung, H. Y. Jeong, J.-S. Lee, M. G. Kim, J. Cho, *Angew. Chem. Int. Ed.* **2014**, *53*, 4582–4586; *Angew. Chem.* **2014**, *126*, 4670–4674.

[14] Y. Li, M. Gong, Y. Liang, J. Feng, J.-E. Kim, H. Wang, G. Hong, B. Zhang, H. Dai, *Nat. Commun.* **2013**, *4*, 1805.

[15] a) Y.-G. Guo, J.-S. Hu, L.-J. Wan, *Adv. Mater.* **2008**, *20*, 2878–2887; b) F. Cheng, J. Shen, B. Peng, Y. Pan, Z. Tao, J. Chen, *Nat. Chem.* **2011**, *3*, 79–84.

[16] X. Xu, S. Jiang, Z. Hu, S. Liu, *ACS Nano* **2010**, *4*, 4292–4298.

[17] a) L. Lai, J. R. Potts, D. Zhan, L. Wang, C. K. Poh, C. Tang, H. Gong, Z. Shen, J. Lin, R. S. Ruoff, *Energy Environ. Sci.* **2012**, *5*, 7936–7942; b) D. Geng, Y. Chen, Y. Chen, Y. Li, R. Li, X. Sun, S. Ye, S. Knights, *Energy Environ. Sci.* **2011**, *4*, 760–764; c) V. Chabot, D. Higgins, A. Yu, X. Xiao, Z. Chen, J. Zhang, *Energy Environ. Sci.* **2014**, *7*, 1564–1596.

[18] a) J. Masa, W. Xia, I. Sinev, A. Zhao, Z. Sun, S. Grützke, P. Weide, M. Muhler, W. Schuhmann, *Angew. Chem. Int. Ed.* **2014**, *53*, 8508–8512; *Angew. Chem.* **2014**, *126*, 8648–8652; b) Y. Liang, H. Wang, J. Zhou, Y. Li, J. Wang, T. Regier, H. Dai, *J. Am. Chem. Soc.* **2012**, *134*, 3517–3523.

[19] Y. Liang, Y. Li, H. Wang, J. Zhou, J. Wang, T. Regier, H. Dai, *Nat. Mater.* **2011**, *10*, 780–786.

[20] a) J. Jiang, Y. Li, J. Liu, X. Huang, C. Yuan, X. W. Lou, *Adv. Mater.* **2012**, *24*, 5166–5180; b) Z.-L. Wang, D. Xu, J.-J. Xu, X.-B. Zhang, *Chem. Soc. Rev.* **2014**, *43*, 7746–7786.

[21] D. U. Lee, H. W. Park, M. G. Park, V. Ismayilov, Z. Chen, *ACS Appl. Mater. Interfaces* **2015**, *7*, 902–910.

[22] G.-L. Tian, M.-Q. Zhao, D. Yu, X.-Y. Kong, J.-Q. Huang, Q. Zhang, F. Wei, *Small* **2014**, *10*, 2251 – 2259.

[23] D. U. Lee, M. G. Park, H. W. Park, M. H. Seo, X. Wang, Z. Chen, *ChemSusChem* **2015**, *8*, 3129 – 3138.

[24] a) X. Xie, Y. Li, Z.-Q. Liu, M. Haruta, W. Shen, *Nature* **2009**, *458*, 746 – 749; b) Y. Wang, C. M. Yang, W. Schmidt, B. Spliethoff, E. Bill, F. Schüth, *Adv. Mater.* **2005**, *17*, 53 – 56.

[25] a) X. Wang, X. Fan, G. Li, M. Li, X. Xiao, A. Yu, Z. Chen, *Carbon* **2015**, *93*, 258 – 265; b) X. Wang, G. Li, R. Tjandra, X. Fan, X. Xiao, A. Yu, *RSC Adv.* **2015**, *5*, 41179 – 41185; c) X. Wang, G. Li, M. H. Seo, F. M. Hassan, M. A. Hoque, Z. Chen, *Adv. Energy Mater.* **2015**, *5*, 1501106.

[26] B. Kumar, M. Asadi, D. Pisasale, S. Sinha-Ray, B. A. Rosen, R. Haasch, J. Abiade, A. L. Yarin, A. Salehi-Khojin, *Nat. Commun.* **2013**, *4*, 0.

[27] a) S. Wang, E. Iyyamperumal, A. Roy, Y. Xue, D. Yu, L. Dai, *Angew. Chem. Int. Ed.* **2011**, *50*, 11756 – 11760; *Angew. Chem.* **2011**, *123*, 11960 – 11964; b) G. Nam, J. Park, S. T. Kim, D.-b. Shin, N. Park, Y. Kim, J.-S. Lee, J. Cho, *Nano Lett.* **2014**, *14*, 1870 – 1876.

[28] X. W. Lou, D. Deng, J. Y. Lee, J. Feng, L. A. Archer, *Adv. Mater.* **2008**, *20*, 258 – 262.

[29] S. Cobo, J. Heidkamp, P.-A. Jacques, J. Fize, V. Fourmond, L. Guetaz, B. Jousselme, V. Ivanova, H. Dau, S. Palacin, M. Fontecave, V. Artero, *Nat. Mater.* **2012**, *11*, 802 – 807.

Received: January 22, 2016
Revised: February 17, 2016